Neurocomputing 194 (2016) 227–240

Contents lists available at ScienceDirect

Neurocomputing

journal homepage: www.elsevier.com/locate/neucom

# 3-Points Convex Hull Matching (3PCHM) for fast and robust point set registration

Jingfan Fan [a], Jian Yang [a,*], Feng Lu [b], Danni Ai [a], Yitian Zhao [a], Yongtian Wang [a]

[a] Beijing Engineering Research Center of Mixed Reality and Advanced Display, School of Optics and Electronics, Beijing Institute of Technology, Beijing 100081, China

[b] School of Computer Science and Engineering, and International Research Institute for Multidisciplinary Science, Beihang University, Beijing 100191, China

ARTICLE INFO

*Article history:*
Received 9 October 2015
Received in revised form
1 January 2016
Accepted 24 January 2016
Available online 3 March 2016

*Keywords:*
Convex hull
Point sets
Registration
Shape matching

ABSTRACT

Point set registration plays a crucial role in numerous computer vision applications. This paper proposes a novel and general approach called three-point convex hull matching (3PCHM) for registering two point sets with similarity transform. First, convex hulls are extracted from both point sets. Triangular patches on the surface of convex hulls are specified by predefining their normal vectors, thus guaranteeing that all points are located on the same side of any randomly selected triangle plane. Second, the potential similar triangle pair set is obtained by comparing the length ratio of the edges on the two extracted convex hulls. Thereafter, the transformation parameters for each pairwise triangle are calculated by minimizing the Euclidean distance between the corresponding vertex pairs. Furthermore, a k-dimensional (k-d) tree is used to accelerate the closest point search for the whole point sets. Third, outliers that may lead to significant errors are discarded by integrating the random sample consensus algorithm for global optimization. Experiments show that the proposed 3PCHM is robust even with the existence of noise and outliers and is effective in cases of part-to-part registration and part-to-whole registration.



## 1. Introduction

The development of computer graphics, computer vision, virtual reality, and augmented reality in recent years has increased the research attention on 3D model generation and manipulation techniques. In all relative techniques, registration and alignment are the most important aspects for the quantitative analysis of 3D models. A 3D model can be represented as a mesh or cloud point, and the registration technique aims to find the best matching geometric warping among models at different representations. This technology has significant applications in the fields of photogrammetry, motion tracking, camera pose recovering, and object identification.

In the past two decades, numerous methods have been developed for the registration of point sets and 3D models. The most famous method is the iterative closest point (ICP), which was proposed by Besl and Mckay [1] in 1992. In ICP, the transformation between two different point sets is optimized by minimizing Euclidian distance between every corresponding point pair of two sets. Considering the simplicity and effectiveness of ICP for point sets with relatively small variations, ICP has been widely used in different fields and referenced by numerous studies. However, the ICP algorithm is highly dependent on the initial geometry of registering point sets and can be easily trapped into a local minimum.

Numerous ICP variants have greatly increased our understanding of matching problems. The ICP algorithm generally assumes that the points to be registered have homogeneous Gaussian noise. On the basis of this hypothesis, Granger et al. [2,3] extended the ICP algorithm by using expectation-maximization (EM) principles to estimate the Gaussian weights of the matches, thus resulting in the EM–ICP algorithm. They also proposed a coarse-to-fine annealing scheme to avoid local minimum. By decimating the point sets, the computation time explosion at coarse levels can be reduced. EM–ICP provides better repeatability, superior accuracy, and higher computation efficiency than the original ICP. Instead of calculating the one-to-one corresponding relationship between each point by using the nearest neighbor criterion, Myronenko [4,5] and Jian et al. [6] assumed that each model point corresponds to a weighted sum of the scene points; thus, the point sets can be represented as Gaussian mixture models (GMMs). Point set registration can also be used to align two Gaussian mixtures by minimizing their discrepancies. Rather than providing additional prior affinity measures [7] for ICP algorithms, GMM-based algorithms [8] statistically estimate the

* Corresponding author.
*E-mail address:* jyang@bit.edu.cn (J. Yang).

http://dx.doi.org/10.1016/j.neucom.2016.01.078
0925-2312/

discrepancy between point sets and significantly improve the computational accuracy and robustness of point set registration.

ICP variants generally employ the Euclidean distance as the distance metric. The Euclidean distance theoretically guarantees that corresponding matches can be found by tentative iterations. However, some of these algorithms are rendered ineffective by noise, occlusion, and partial point scarcity. An effective way to modify the distance metric with respect to the whole point set is to find local invariant features [9], such as surface orientation [10], curvature [11], and normal [12] or congruent shapes [13]. Some algorithms aim to establish a pairwise relationship and distinguish a limited number of invariable features from numerous points with respect to similarity transformation, thus resulting in a significant reduction in computation complexity. However, feature extraction and matching procedures are sensitive to imaging noise and resolution. Thus, higher levels of geometric descriptors such as shape contexts [14,15], spin images [16], similarity graphs [17], and log-polar height maps [18] have been proposed for point set registration. These approaches generally integrate structural or topological information into the registration scheme, thus allowing the accurate estimation of camera parameters under poor initialization and the handling of partial or missing structures. Unfortunately, these techniques are ill suited for point sets with unknown densities or sparse distributions. Furthermore, localization uncertainty for point sets may be highly anisotropic because of different imaging techniques. Therefore, the commonly assumed isotropic noise distribution for point sets can be deemed as an ill-posed theorem, thus leading to the use of SoftICP [19], SoftAssign [20], or A-ICP [21] for the estimation and refinement of tentative correspondences by the integration of anisotropic weight estimation.

Given that iterative optimization is needed to minimize the sum of squared distances between corresponding points, several strategies have been designed to improve the effectiveness of registration procedures (e.g., the Levenberg–Marquardt (LM) algorithm [22], dynamic programming [23,24], annealing scheme [25], and multi-resolution strategies [26]). The LM–ICP [22], which is capable of yielding a large basin of convergence than common techniques, is proposed by integrating the LM algorithm into the optimization kernel function. The random sample consensus (RANSAC) algorithm [27] iteratively estimates the parameters of a predefined model of observed data by removing outliers; this method is effective for refining the results of point set registration [28,29]. The four-point congruent sets (4PCS) approach is proposed by extracting all coplanar four-point set from source point sets that are approximately congruent to the given set of coplanar four-point in the target point sets under rigid transformation [13]. By integrating the RANSAC algorithm, the 4PCS is capable of calculating the global transformation by using a set of sampling coplanar points. On the contrary, recent developments in graphics hardware and software have motivated people to accelerate registration procedures by parallelization [30] and graphics processing unit (GPU) [31] implementations, which have been widely acknowledged as effective ways for fast registration.

All of the above-mentioned methods have greatly improved the technique of point set registration. However, given that the complexity of the registration problem is closely correlated with the noise distribution, density, and sparsity of two point sets, many challenges for robust point set registration still exist. We propose a novel three-point convex hull matching (3PCHM) method on the basis of previous studies. First, convex hulls are extracted from both point sets to be registered. The specification of triangle patches is then conducted by using normal vectors on the convex hulls. Thereafter, a similar triangle pair set is obtained by comparing the length ratio of each triangle on the convex hull of the two point sets; this step also assists the computation of the scaling factor for the similarity transformation. The optimization of the transformation parameters including the rotation and translation for each triangle pair is realized by minimizing the Euclidean distance between the corresponding vertex pairs. Pairs that may lead to significant errors are discarded by using the RANSAC algorithm to achieve global optimization. The main contribution of the proposed algorithm is twofold: first, considering that the invariant property of the extracted 3D convex hull is used for point set registration, the process is independent of the initial pose and the alignment of point sets. Second, the registration procedure is robust and efficient with respect to the initial transformation because of the utilization of limited number triangle pairs for computation.

## 2. Method

Suppose we have two finite sized point sets with similarity transformation to be registered. Let $P=\{p_1 p_2,\ldots,p_{N_P}\}$ represent the source point set and $Q=\{q_1,q_2,\ldots,q_{N_Q}\}$ represent the target point set. Both $P$ and $Q$ are assumed subsets of the vector space $\mathbb{R}^3$, $N_P$ and $N_Q$ are the number of $P$ and $Q$ respectively. The registration approach is addressed to obtain the optimal transformation between spaces. Fig. 1 shows the basic procedural flow of the 3PCHM algorithm with its key processes. The registration procedure can be divided into the following stages:

a) The first stage is the formation of the convex hull and involves the extraction of the convex hull of both 3D point sets.
b) The second stage is triangle matching, wherein the length ratios of each triangle are computed and ordered. Thereafter,

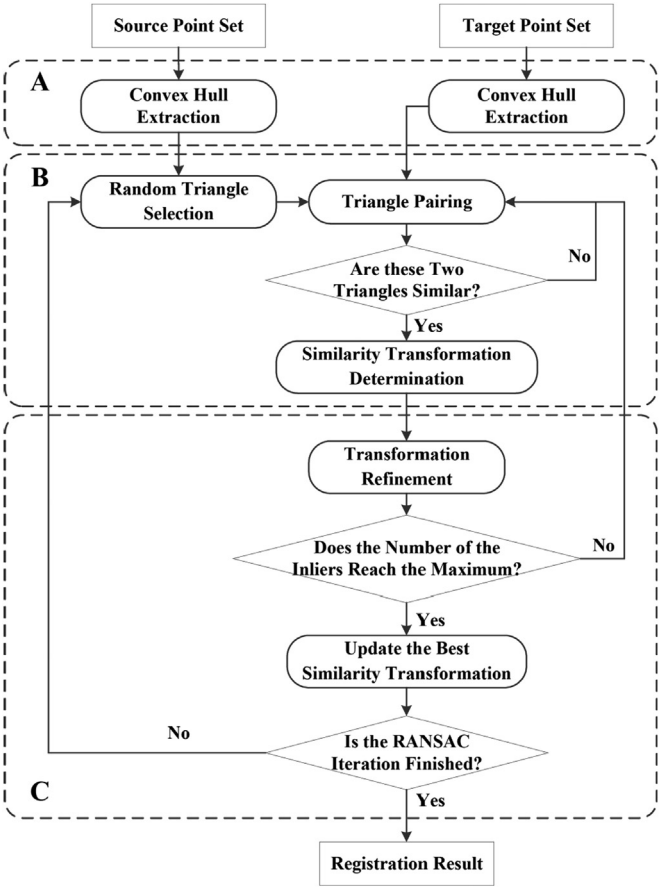


**Fig. 1.** Flow chart of the 3PCHM algorithm. (A) Formation of convex hull. (B) Triangle matching and registration. (C) Global optimization.

similar triangles are paired by comparing the length ratio vectors.

c) For the third stage, the above procedure is conducted iteratively for all possible triangle pairs for both sets to obtain the most similar pair that can yield the best possible similarity transformation. Both point sets are then affined with this transformation.
d) Thereafter, this transformation is optimized iteratively by using the RANSAC global optimization method until the number of inliers reaches the maximum. The optimization proceeds to guarantee that the number of outliers is minimized by this phase in every recursion.
e) The output of the proposed algorithm is the final registration result obtained by registering the two point sets by using this optimized transformation.

### 2.1. Formation of the convex hull

The convex hull of a set of 3D points is the minimum convex combination that contains all points, which are commonly used to represent the extension ranges of the point sets. The convex hull of a point set has the following three properties:

a) The convex hull is unique for a defined point set.
b) The structure of the convex hull is affine invariant.
c) The calculation of convex hull is simple and fast.

Therefore, the convex hull is suitable for registering point sets by affine transformations because point sets are usually polluted by amplitude noises or outliers, which may change the topological structure of the convex hull. We first denoised the inputs by classifying the distances of local neighboring points. If the distance between two closing points is considerably larger than the distance of a neighboring point, the neighboring point is deemed as an outlier and is removed. Thus, the convex hull from the point sets can be guaranteed consistent and uniform. Fig. 2(a) shows the extraction of the convex hull of the curved surface. The first figure in Fig. 2(a) depicts convex hull $S_1$, wherein two triangles (*ABC* and *BCD*) are chosen on the surface of the convex hull. The next figure in the first row shows the zoomed out figure of the same convex hull $S_1$ depicted as $S_2$. The figure shows that the concept of convex hull is independent of scaling and rotation as triangles $A'B'C'$ and $B'C'D'$ remains the same as *ABC* and *BCD*. The first column in Fig. 2 (b) shows the 3D visualization of the bunny set followed by the extracted convex hull and a chosen triangle on the surface of the convex hull of the bunny set.

For a finite size point set: $P \in \mathbb{R}^3$, $S(P)$ define the convex polyhedron surface consisting of all points in point set $P$ and can be represented as follows:

$$S(P) = \{p \mid p \in P \,\&\, p \notin S(P - \{p\})\} \tag{1}$$

Point $p$ in $P$ is considered the vertex of $S(P)$ if $p$ satisfies the following condition:

$$p \notin S(P - \{p\}) \tag{2}$$

From the above equations, the convex hull of $P$ is represented as the convex polyhedron based on the vertices in $\mathbb{R}^3$. In the proposed approach, the convex hull is considered the finite set of directed triangle facets. A directed triangle facet $F$ can be represented by using three sequential vertices: $v_A$, $v_B$, and $v_C$. Furthermore, the cross product of the ordered vertices is denoted by $\overrightarrow{Norm_F}$ and can be described as follows:

$$\overrightarrow{Norm_F} = (v_B - v_A) \times (v_C - v_B) \tag{3}$$

The definition of the ordered points must satisfy that the cross product $\overrightarrow{Norm_F}$ of the vertices denotes the inner side of the whole point sets and in the right-handed coordinate system. Thereafter, the directed triangle facet $F$ can be parameterized as follows:

$$F = \left\{ v_A, v_B, v_C, \overrightarrow{Norm_F} \middle| v_A, v_B, v_C \in V(P) \right\} \tag{4}$$

where $V(P)$ means the vertices of the convex hull of $P$.

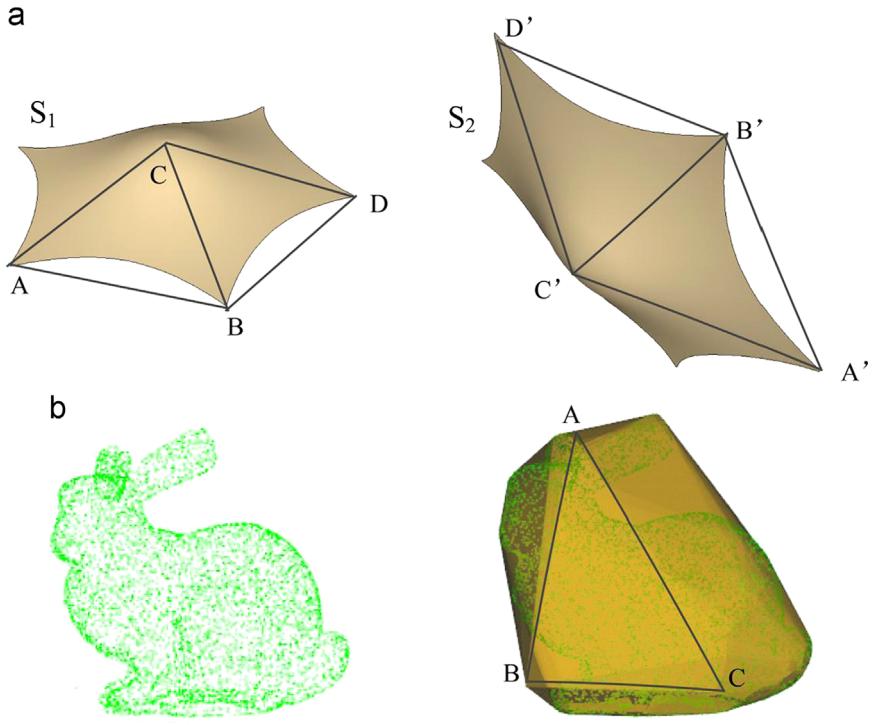


**Fig. 2.** Schematic of the convex hull extracting procedure. (a) Shows the convex hull extraction for a curved surface in different location. (b) Shows the visualization of the bunny point set, its corresponding convex hull, and a triangle for matching on the convex hull.

In computation geometry, the convex hulls can be attained effectively by numerous algorithms. Computation geometry involves tracing the most efficient and clearest description of the convex polyhedron. The output-sensitive-based procedure [32] is applied to obtain the 3D convex hull. The observed computational complexity is $O(n \log h)$, where $h$ denotes the number of facets of the corresponding convex hull and $n$ is the number of points in the point cloud $P$. Fig. 2(b) depicts the convex hull extraction of the Stanford Bunny point set [33]. The figure shows the bunny point set followed by the actual shape of the point set in 3D space and the extracted convex hull with a triangle chosen randomly on the surface of the convex hull.

### 2.2. Triangle matching and registration

A partial triangle matching approach is proposed to identify the correspondences between the two point sets once the extraction of the convex hull is performed. Matching all points in the two point sets directly is computationally expensive and difficult. Thus, the matching of two triangles on the convex hulls of both the point sets is conducted to obtain the best transformation result for the given pair of sets. To find the matching triangles in both point sets, the following procedure is applied:

a) The length of the edge for each triangle is calculated and ordered. The ratios of the three edges, including the maximum to minimum, maximum to median, and median to minimum, are also calculated to form the length ratio vectors.
b) The triangle in point set $P$ is matched with the triangle in point set $Q$ to find a similar triangle with the minimum Euclidean distance error of the length ratio vector.

The optimization procedure will be skipped if the two triangles are dissimilar within the tolerant error. The proposed approach will not enumerate all triangles, thus greatly improving the computational efficiency.

Suppose $\{p_i\}$ and $\{q_i\}$; $i=1,2,3$ are vertices of two triangles from point sets $P$ and $Q$, respectively. The registration procedure will then involve the identification of the similarity transformation $T(R,\vec{t},s)$ that provides the minimum square value of the Euclidian distance between the following two triangles:

$$T^* = \arg\min_{R,\vec{t},s} \frac{1}{n}\sum_{i=1}^{n} \|q_i - (sRp_i + t)\|^2 \tag{5}$$

where $\vec{t}$ is a $3\times 1$ translation vector, $\mathbf{R}$ is a $3\times 3$ rotation matrix, $s$ is the scaling factor, and n is the number of vertices. The rotation matrix $\mathbf{R}$ can also be parameterized by three rotation angles, namely, $\theta_\alpha$, $\theta_\beta$, and $\theta_\gamma$, with respect to the $x$, $y$, and $z$ axes. The translation vector $\vec{t}$ can be parameterized by $t_x$, $t_y$, and $t_z$ with respect to the $x$, $y$, and $z$ axes, respectively. The similarity transformation can then be defined with seven unknown parameters as follows:

$$T(R,\vec{t},s) = \begin{bmatrix} \cos\theta_\beta \cos\theta_\gamma \cdot s & \sin\theta_\alpha \sin\theta_\beta \cos\theta_\gamma - \cos\theta_\alpha \sin\theta_\gamma & \cos\theta_\alpha \sin\theta_\beta \cos\theta_\gamma + \sin\theta_\alpha \sin\theta_\gamma & t_x \\ \cos\theta_\beta \sin\theta_\gamma & \sin\theta_\alpha \sin\theta_\beta \sin\theta_\gamma + \cos\theta_\alpha \cos\theta_\gamma \cdot s & \cos\theta_\alpha \sin\theta_\beta \sin\theta_\gamma - \sin\theta_\alpha \cos\theta_\gamma & t_y \\ -\sin\theta_\beta & \sin\theta_\alpha \cos\theta_\beta & \cos\theta_\alpha \cos\theta_\beta \cdot s & t_z \\ 0 & 0 & 0 & 1\cdot s \end{bmatrix} \tag{6}$$

**Table 1**
Pseudocode for Algorithm 1.

**Algorithm 1**: STM (Similar triangles matching)

**Input**: Two triangles $\{p_i\}$ and $\{q_j\}$.
**Output**: The best similarity transform $T^*_{i,j}$ between the similar triangle pair.
1: Calculate the lengths of the edges which form the length vectors in decreasing order, we have $\{l_1^p, l_2^p, l_3^p\}$ and $\{l_1^q, l_2^q, l_3^q\}$; $l_1^p \ge l_2^p \ge l_3^p$, $l_1^q \ge l_2^q \ge l_3^q$.
2: Calculate the ratio vectors of the lengths, we have $\{r_1^p, r_2^p, r_3^p\} = \left\{\frac{l_1^p}{l_3^p}, \frac{l_1^p}{l_2^p}, \frac{l_2^p}{l_3^p}\right\}$ and $\{r_1^q, r_2^q, r_3^q\} = \left\{\frac{l_1^q}{l_3^q}, \frac{l_1^q}{l_2^q}, \frac{l_2^q}{l_3^q}\right\}$.
3: **if** the condition $\|r_1^p - r_1^q\|^2 \approx \|r_2^p - r_2^q\|^2 \approx \|r_3^p - r_3^q\|^2$ is in a minimal predefined threshold value $\delta$ **then**
4: Calculate the scale of these two triangles
$$s = average\left(\frac{l_1^p}{l_1^q}, \frac{l_2^p}{l_2^q}, \frac{l_3^p}{l_3^q}\right)$$
5: **else**
6: **return** matching false
7: **end if**
8: Calculate the best similarity transform by Eq. (5)
9: **return** $T^*$

The alignment task for the two triangles can be solved by the least-squares estimation method developed in [34].

If all points are used to optimize the transformation relationship during the registration process, the amount of calculation will be large for dense point sets. To improve the registration efficiency and reduce the influence of initial estimation, this study employs the principle of the local matching algorithm to realize the global registration of the whole point sets. Considering that three points are the basis component for registration, we randomly extract three adjacent points on the convex hull of point set $P$. The composed triangle is then matched with the triangle in $Q$ by determining the length ratio. Thus, all matching can provide an optimized transformation, which is then further used to perform the global optimization of the whole point sets by RANSAC optimization. The detail is shown in Table 1.

### 2.3. Global optimization

According to the above calculation procedure, every triangle in point set $P$ is paired with a triangle in point set $Q$ on the basis of a similar property. Furthermore, we can obtain a transformation T for each matching pair. The total number of transformation for point sets $P$ and $Q$ is $N_P \times N_Q$. However, because of noise interference and local structure deformation, many false triangles may be included for matching. To improve the registration accuracy, the RANSAC optimization method is used to remove false matching triangles in this section. The RANSAC algorithm, proposed by Fischler et al. [27], is a general parameter estimation approach designed to extract inlier models, which can effectively restrain the influence of noise and singular point, from the input data. The principle idea of RANSAC optimization is to remove correspondence pairs that may lead to large matching errors of the whole point sets. The optimization process can be defined as follows:

**Table 2**
Pseudocode for Algorithm 2.

**Algorithm 2**: 3PCHM (3-Points Convex Hull Matching)

**Input**: Two point sets $P$ and $Q$ with arbitrary position and orientation having cardinality $N_P$ and $N_Q$ respectively.
**Output**: The best similarity transform $T_{opt}$ leading the minimum Euclidean distance between the two point sets $P$ and $Q$.

```
Set the initial max number of inliers τ←0.
S(P)←CalculateConvexHull(P)
S(Q)←CalculateConvexHull(Q)
Build initial k-d tree of point set P
for i=1 to L do {RANSACLOOP}
    B←RandomSelectTriangle(S(P))
    for all triangle facets F_j ∈ S(Q) do
        T_j←STM(B,F_j) (using Algorithm 1)
        Find inlier point set C_inlier
        if n(C_inlier) > τ then
            Update the max number of inliers
            τ←n(C_inlier)
            Update the best transform matrix
            T_opt←T_j
        end if
    end for
end for
return T_opt
```

a) In every iteration step, three noncollinear random pairs of correspondences on the convex hull are extracted to refine the matching transformation defined in Eq. (5).
b) The obtained transformation $T^*$ is used to transform the vertex of the source point sets to the target coordinates. Thereafter, the similarity of the two point sets can be obtained and recorded.
c) The inlier and outlier correspondences are classified by the following thresholding function:

$$c(v_i^P) \in \begin{cases} C_{inlier}, & \left\| T^*(v_i^P) - v^Q_{c(v_i^P)} \right\| \le \delta \\ C_{outlier}, & else \end{cases}, \quad i = 1, \ldots, N_{V(P)} \tag{7}$$

where $\|\cdot\|$ is the Euclidean distance between two closet points, wherein the corresponding index $c(v_i^P)$ of the closet point of $v^Q_{c(v_i^P)}$ to the transformed point $v_i^P$ is calculated by the k-dimensional (k-d) tree classification.

a) All inlier correspondences are used to optimize the best transformation between the two point sets. The number of inlier correspondences of the current iteration is recorded as $\tau_i$.
b) For every iteration step, current $\tau_i$ is compared with the previous iteration $\tau_{i-1}$, which is used to validate the effectiveness of the current calculation step.
c) The calculation is terminated until we obtain the maximum number of inlier correspondences. The more details are shown in Table 2.

For our registration technique, the RANSAC algorithm is integrated into the registration process to optimize the global transformation between the two point sets. For each triangle in $P$, we find a matching triangle in $Q$ and obtain the best transformation $T_i$ between two triangles. To evaluate the validity of each transformation, we calculate the Euclidian distance of every point between $T_i(P)$ and $Q$ and record the number of points with the distance error less than a predefined threshold of $\delta$. In this study, the closed point query is calculated by using the k-d tree based algorithm [35], which has a calculation efficiency of about $O(\log_2 N_Q)$. The integrated RANSAC algorithm can guarantee global transformation by randomly extracting triangles on the convex hull and registering them together. When the iteration proceeds, the transformation $T_{opt}$ with the maximum number of inlier points is adopted as the best transformation between these two point sets.

**Table 3**
Transformation parameters for the simulated data.

| Categories | Parameters | Range |
|---|---|---|
| Rotation | $\theta_\alpha, \theta_\beta$ and $\theta_\gamma$ | [30°,60°] |
| Translation | $t_x, t_y$ and $t_z$ | [100,300] |
| Scale | $s$ | [0.8,1.2] |
| Noise | $\sigma$ | 2.0 |

## 3. Experimental results

To evaluate the performance of the proposed algorithm, a series of experiments on simulated data sets is designed to test the effectivity and robustness of the algorithm on different noise scales, initial rotational angles, and scaling factors. Moreover, a series of data sets are simulated to evaluate the effectivity of our algorithm on partial registration and part-to-whole registration. The registration accuracy is evaluated by the root-mean-square (RMS) error, which is calculated as the summary of the Euclidian distances of every corresponding point pair between the source and target point sets. Furthermore, experiments are designed to evaluate the recovery abilities of the transformation parameter. For each designed experiment, our algorithm is compared with the LM–ICP [22], EM–ICP [2,3], and 4PCS [13] algorithms as mentioned in the first section. Without loss of generality, the simulated data sets are generated by the parameter ranges listed in Table 3. For each designed experiment, the source point set is randomly selected from the publicly available point set repository. The target point set is then generated from the source point sets by using the randomly generated parameters in the predefined ranges. The programming environment is UNIX, and all experiments are performed on a relatively low cost PC with 16 GB RAM and a 3.4 GHz Intel CPU.

The range of the parameters is selected while considering the following scenarios: first, the angle of rotation is chosen to be in the range of [30°, 60°] because we want to compare the relative performance of different algorithms in different situations such as partial or part-to-whole registration. Some algorithms do not function in cases when the rotation angle is higher than 60°. Thus, we try to select a range that can obtain results for every algorithm in this study to obtain reasonable analysis results. Second, for choosing a range for translation, we set the range at [100, 300]. This range is selected because our data has been already normalized on the scale of 0 to 100. To avoid the overlapping and interpolation of data and to check the performance of the algorithm in practical difficulties, the range is chosen as above. As far as scaling is concerned, we decide to use a scaling factor of 20%. Thus, the range is chosen to be 20% zoomed in to 20% zoomed out to the actual scaling of the point. These chosen ranges are reasonable enough for practical experimentation after the comparative study.

Fig. 3 shows the performance of 3PCHM in the presence of noise and outliers. The frog data set is obtained from the Aim@-SHAPE Shape Repository [36]. The blue image shows the original point set, whereas the next images of red point sets are generated by randomly translating every point of the frog data in 3D space. The translations for each point in the three axis of the frog data are independent and the amount of translation is under controlled Gaussian distribution with standard deviations of $\sigma = 1.0$, $\sigma = 2.0$, $\sigma = 4.0$, and $\sigma = 8.0$. In the registration result, the appearance of

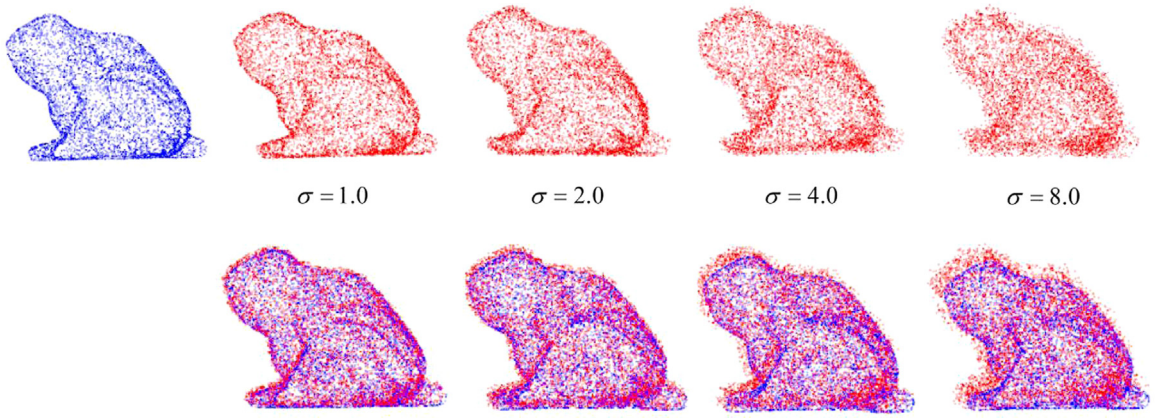


**Fig. 3.** Registration results of point sets with varying noise scales. Top row: source point set (left blue points) and target point sets (right red points), which are generated from the source point with a different scale of noise $\sigma$. Bottom row: registration results of the source and target point sets. (For interpretation of the references to color in this figure legend, the reader is referred to the web version of this article.).

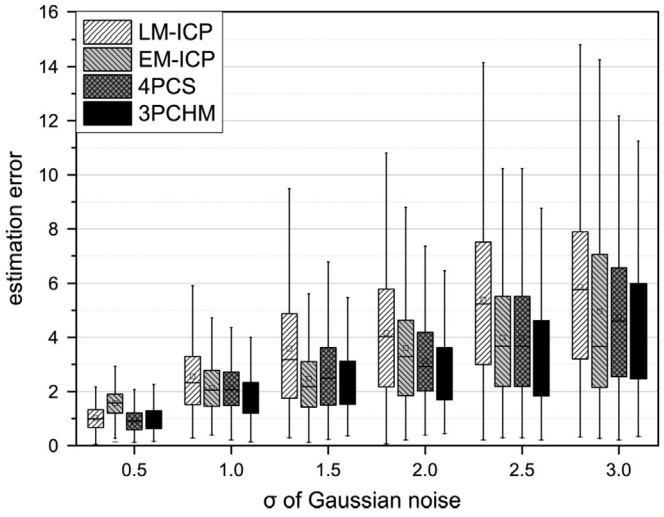


**Fig. 4.** Comparison of different algorithms over varying scales of Gaussian noises.

the color purple is due to the overlapping of the blue and red point sets. The experiment shows that the number of outlier increases with increasing noise levels. However, the result of the registration procedure is still accurate and is unaffected by the presence of noise.

Fig. 4 shows the relative performance of 3PCHM in the presence of noise and outliers with LM–ICP, EM–ICP, 4PCS, and 3PCHM. The mean of the box plots helps relate the estimated errors of all methods with increasing Gaussian noise levels. The estimated error increases considerably for LM–ICP and EM–ICP with increasing noise levels. One major observation in this result is the increase in the error for 4PCS; however, the magnitude increases insignificantly. The same result applies to the proposed 3PCHM algorithm. The mean errors estimated at $\sigma = 0.5$ for LM–ICP, EM–ICP, 4PCS, and 3PCHM are 1.01, 1.65, 0.90, and 0.94, respectively; the errors estimated for the aforementioned methods are 5.87, 3.71, 4.68, and 4.12, respectively, with maximum error encountered of 14.85, 14.37, 12.21, and 11.28, respectively (Fig. 4). The increase in estimated error for 3PCHM is minimal compared with all other methods.

Fig. 5 shows the effect of rotation on algorithm performance. The Buste point data is obtained from the Aim@SHAPE Shape Repository [36]. Fig. 5 shows the registration results between a static source point set and another point set that is rotated at an angle in the range of [0°, 180°] with a difference of 30°. The distance maps show the estimation error directly. The mesh in green shows the mean error that is limited to zero, and the errors increase as the mesh approaches the color blue or red. The third row shows the zoomed in part of the figure that contains more visible errors than the rest of the figure. Each part shows some red or blue areas where the estimation error is encountered. However, the area the encounters errors is reasonably small compared with the whole figure and that the extremes of the color bar are untouched, that is, the error is not located on the extremes of the error scale. The max error estimated is below 2.5 units.

Fig. 6 shows the estimated error of 3PCHM compared with LM–ICP, EM–ICP, and 4PCS against the rotational angle. The figure shows that the error estimated for both LM–ICP and EM–ICP increases significantly with increasing rotational angle. The mean errors estimated at 60° for LM–ICP, EM–ICP, 4PCS, and 3PCHM are 2.83, 2.15, 1.87, and 1.64 with a maximum possible error being 8.61, 5.79, 4.40, and 4.00, respectively. For the largest possible angle (i.e., 180°), the maximum errors encountered are more than 20.0 for LM–ICP and EM–ICP and more than 4.0 for 4PCS and 3PCHM with a mean error of 5.57, 6.43, 1.78, and 1.61, respectively. The evaluation shows that the performance of 3PCHM is better than LM–ICP, EM–ICP, and 4PCS in rotation cases, and the proposed algorithm is almost unaffected by the rotation of the point set.

Fig. 7 shows the effect of scaling on the performance of all algorithms. The error estimated increases from a maximum of 12.43 for a 0.5 scaling factor to 18.77 for a scaling factor of 3.0 for LM–ICP. The same pattern applies to EM–ICP and 4PCS. For 3PCHM, the pattern ranges from a maximum of 4.91 for a 0.5 scaling factor to 4.27 for a 3.0 scaling factor. This amount is considerably small compared with the estimated error for other algorithms. The mean errors estimated for LM–ICP, EM–ICP, 4PCS, and 3PCHM at a scaling factor of 0.5 are 4.37, 3.01, 2.38, and 2.07. At a scaling factor of 3.0, the errors are 5.79, 4.08, 1.85, and 1.73 with a maximum error of 18.74, 10.97, 5.02, and 4.30, respectively.

Fig. 8 shows the registration results for different sampling densities. The Happy Buddha data set is obtained from the Stanford 3D Scanning Repository [33]. The different sampling densities of the point sets are obtained by choosing a specific percentage of points from the whole point set and applying random translation, rotation, and scaling in the predefined range. Fig. 8 indicates that the color of the last entry is the brightest of all results because the last entry has 80% of the points in one set and 100% in the other. The accurate registration results obtained with 3PCHM shows the efficiency of the proposed algorithm.

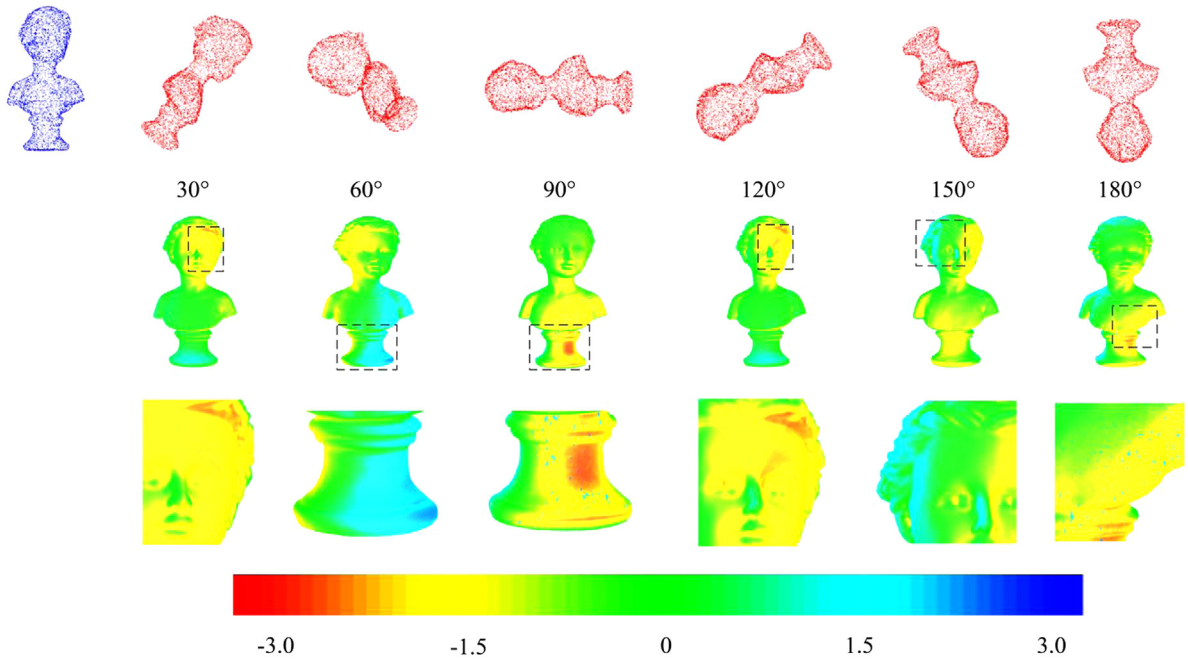


**Fig. 5.** Registration of point sets with varying initial rotational angles. First row: source point set (left blue points) and target point sets (right red points) with 30° to 180° rotation angles. Second row: color map rendering of the distance error between the source and registered point sets over point sets with varying initial rotation angles. Third row: partially enlarged figures that correspond to the rectangular areas in the second row. (For interpretation of the references to color in this figure legend, the reader is referred to the web version of this article.)

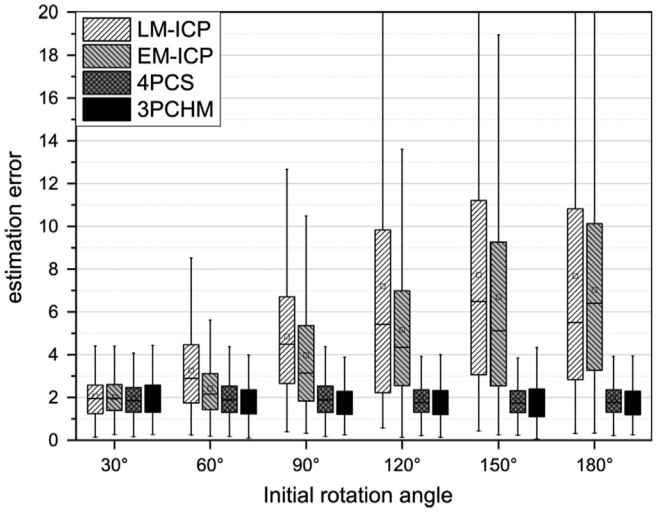


**Fig. 6.** Comparison of different algorithms over varying scales of initial angles.

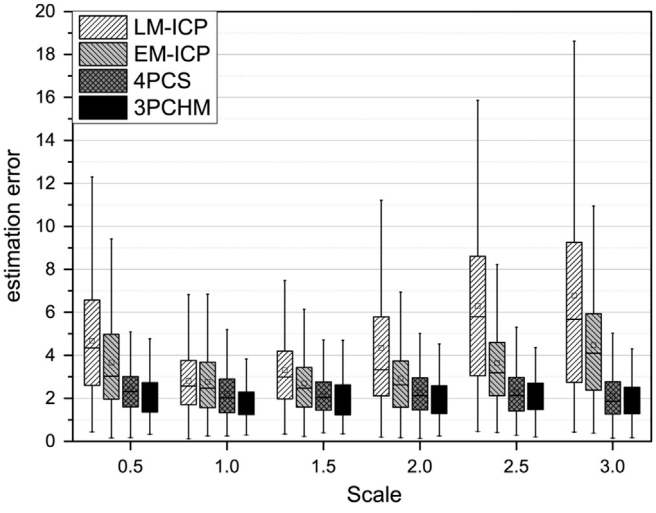


**Fig. 7.** Comparison of different algorithms over varying scaling factors.

Fig. 9 shows the performance of LM–ICP, EM–ICP, 4PCS, and 3PCHM for different sampling densities. The box plots illustrate that the performance of LM–ICP, EM–ICP, and 4PCS exhibits high variations when the density is low (approximately 10–40%). After the density increases from 40% to 100% and the set tends nears completion, the performance of LM–ICP and EM–ICP improves, thus showing the efficiency of these methods. For 10% of the sampling density, the mean errors estimated for LM–ICP, EM–ICP, 4PCS, and 3PCHM are 4.74, 3.21, 2.23, and 1.90 with a maximum error of 13.38, 8.21, 5.67, and 5.02, respectively. For 100% of the registration of two complete point sets, the mean estimated errors for LM–ICP, EM–ICP, 4PCS, and 3PCHM are 2.61, 1.98, 2.36, and 1.83, respectively.

Fig. 10 shows the performance of 3PCHM in the case of part-to-whole registration. The Lion point data set is obtained from the Aim@SHAPE Shape Repository [36]. The blue point sets in the first row denote the original data set. The second, third, and fourth columns show 10%, 40%, and 70% of the horizontal points of the source point set, respectively, whereas the fifth, sixth, and seventh columns show 10%, 40%, and 70% of the vertical points of the source point set, respectively. The second row shows the registered results of the source to the point sets corresponding to the first row. The purple color in the second row shows the overlapped area. This finding proves that the proposed algorithm is capable of registering point sets with a different ratio of partial point sets to whole point sets. Even under a 10% sampling density for the whole points, the two point sets are registered accurately.

Fig. 11 shows the error distribution of LM–ICP, EM–ICP, 4PCS, and 3PCHM in the case of part-to-whole registration. Considering that the degree of completeness increases for the point set, the estimated error for the registration results is decreased considerably for both LM–ICP and EM–ICP. For 20% part-to-whole registration, the

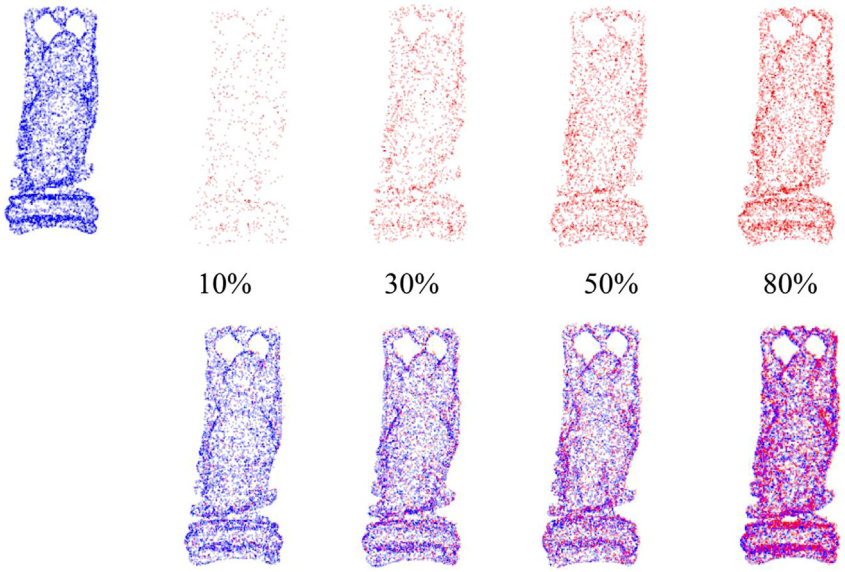


**Fig. 8.** Experimental results of different sampling densities. Top row: source point set (left blue points) and target point sets (right red points) with varying density ratios that correspond to the source point set. Bottom row: registration results of the source and target point sets. (For interpretation of the references to color in this figure legend, the reader is referred to the web version of this article.)

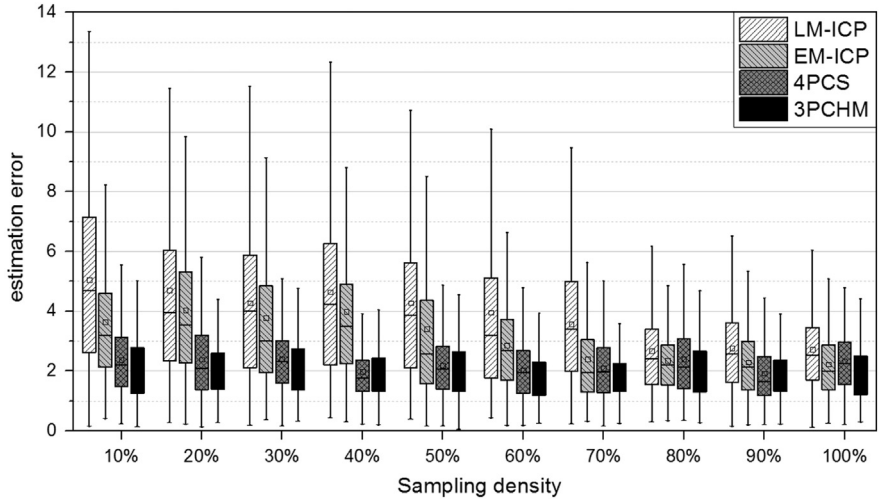


**Fig. 9.** Comparison of different algorithms with varying sampling densities.

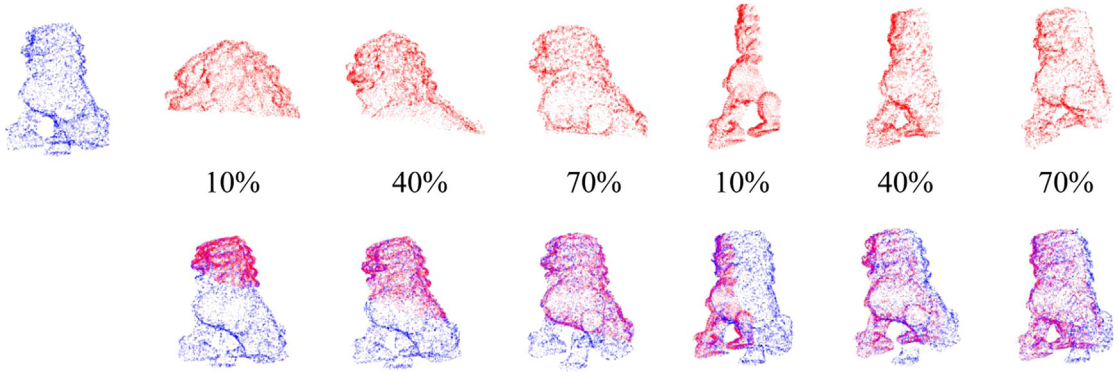


**Fig. 10.** Experimental results of the part-to-whole registration. Top row: source point set (left blue points) and target point sets (right red points) with varying ratios of a random part of the source point set. Bottom row: registration results of the source and target point sets. (For interpretation of the references to color in this figure legend, the reader is referred to the web version of this article.)

mean errors encountered for LM–ICP, EM–ICP, 4PCS, and 3PCHM are 8.73, 7.40, 6.41, and 2.38, respectively. For 100% part-to-whole registration, the maximum errors are 7.37, 5.10, 5.82, and 4.97 for LM–ICP, EM–ICP, 4PCS, and 3PCHM, respectively. Thus, if we try to perform registration by using LM–ICP and EM–ICP for part-to-whole point sets, the error encountered is considerably large. For

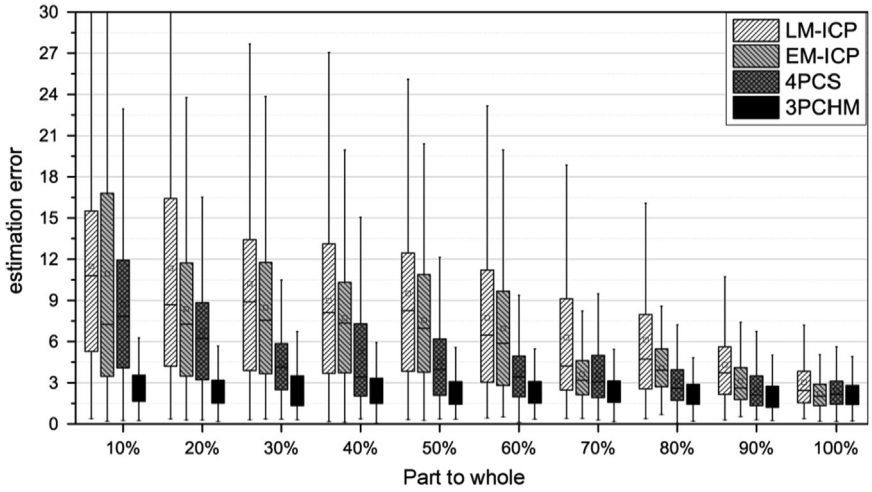


**Fig. 11.** Comparison of different algorithms with varying part-to-whole ratios.

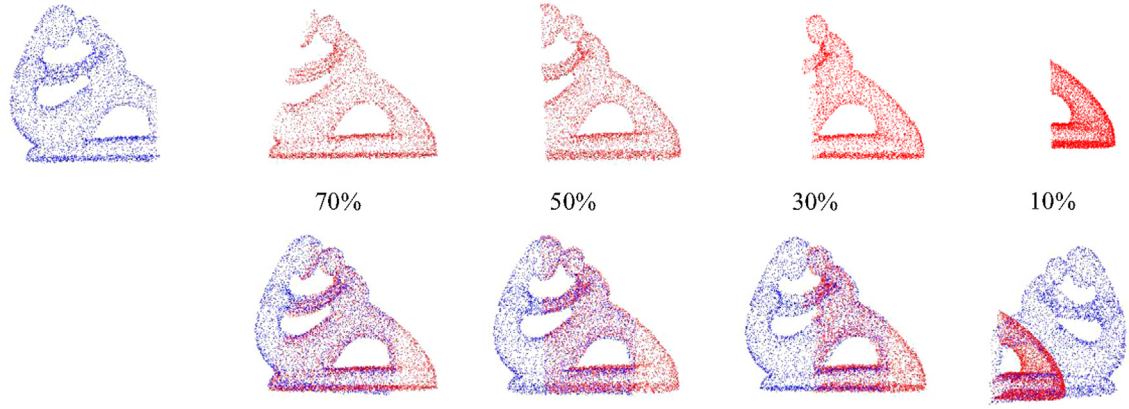


**Fig. 12.** Experimental results of the part-to-part registration. Top row: source point set (left blue points) and target point sets (right red points) with varying overlap ratios. Bottom row: registration results of the source and target point sets. (For interpretation of the references to color in this figure legend, the reader is referred to the web version of this article.)

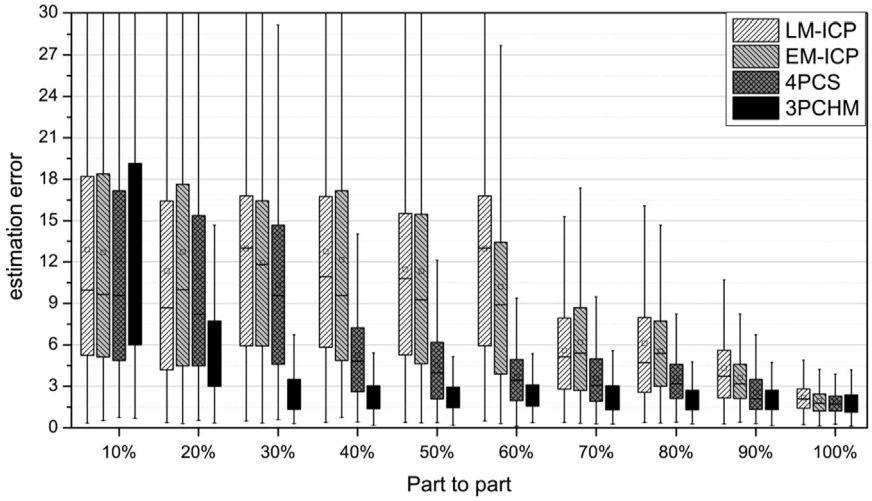


**Fig. 13.** Comparison of different algorithms over varying part-to-part ratios.

4PCS, the same pattern follows this algorithm only with a minor difference with the mean error estimated at each level of the part being analyzed. In case of 3PCHM, the performance is consistent with small errors, which decrease the part of the point set toward completeness.

Fig. 12 shows the performance of 3PCHM in part-to-part registration. The fertility point data set is obtained from the Aim@SHAPE Shape Repository [36]. The blue point set in the first row denotes the original data set, and the right four columns show 10%, 30%, 50%, and 70% overlapped parts for the source point set. The second row shows

the registered results of the source to the point sets corresponding to the first row. The purple color in the second row denotes the overlapped area. This figure indicates that the proposed algorithm performs well with 30%, 50%, and 70% ratio overlapping point sets. However, the registration task fails for 10% overlapping data because the two point sets are registered incorrectly. The result shows that the proposed algorithm requires a certain percentage of overlapping for the two registration point sets, wherein a 10% percent overlap is insufficient for the registration technique.

Fig. 13 shows the error distributions of LM–ICP, EM–ICP, 4PCS, and 3PCHM for part-to-part registration. For 100% overlap data, all four methods reach an accurate registration and the mean errors are lower than 3.0. The four algorithms perform differently with decreasing overlap. Both the LM–ICP and EM–ICP algorithms are sensitive to the overlapping ratios, that is, the registration errors increase significantly with decreasing overlapping ratios. When the overlapping ratio decreases to 60%, LM–ICP and EM–ICP obtain errors larger than 10.0. The 4PCS method works even when the overlapping ratio decreases to 40%, and the mean error maintains an acceptable error of 4.07. The 4PCS is also ineffective for 20% and 30% overlaps. This result shows that the proposed 3PCHM is effective and robust and obtains the minimum registration errors for overlapping rates larger than 20%.

Table 4 shows the performance of transformation parameter estimation for the LM–ICP, EM–ICP, 4PCS, and 3PCHM algorithms in for part-to-whole and part-to-part registrations, wherein algorithms are validated on 50% of points overlapping. In this table, $\theta$, $t$, and s are the estimated rotation, translation, and scaling parameters, respectively; $\widehat{\theta}$, $\widehat{t}$, and $\hat{s}$ are the corresponding grand truths. $\frac{1}{3}\cdot\sum_{\alpha,\beta,\lambda}\frac{|\theta-\hat{\theta}|}{\hat{\theta}}\cdot 100\%$ and $\frac{1}{3}\cdot\sum_{x,y,z}\frac{|t-\hat{t}|}{\hat{t}}\cdot 100\%$ are the relative

**Table 4**
Comparison of the transformation parameter estimation capabilities with varying algorithms for the part-to-whole and part-to-part registrations.

| Arguments/Values/Methods | | $\theta_\alpha$ (deg) | $\theta_\beta$ (deg) | $\theta_\gamma$ (deg) | $\frac{1}{3}\cdot\sum_{\alpha,\beta,\lambda}\frac{\lvert\theta-\hat{\theta}\rvert}{\hat{\theta}}\cdot 100\%$ | $t_x$ | $t_y$ | $t_z$ | $\frac{1}{3}\cdot\sum_{x,y,z}\frac{\lvert t-\hat{t}\rvert}{\hat{t}}\cdot 100\%$ | $s$ | $\frac{\lvert s-\hat{s}\rvert}{\hat{s}}\cdot 100\%$ |
|---|---|---|---|---|---|---|---|---|---|---|---|
| Ground truth | | 30 | 30 | 30 | – | 75 | 75 | 75 | – | 1.20 | – |
| 50% Part to whole | LM–ICP | 30.55 | 45.98 | 20.62 | 61.7% | 73.83 | 76.44 | 77.21 | 3.8% | 1.00 | 16.7% |
| | EM–ICP | 40.15 | 24.3 | 33.42 | 40.4% | 74.15 | 77.96 | 73.74 | 4.4% | 0.97 | 19.2% |
| | 4PCS | 32.71 | 29.99 | 28.12 | 10.9% | 75.27 | 74.70 | 76.23 | 1.7% | 1.18 | 1.7% |
| | 3PCHM | 30.17 | 30.75 | 28.91 | 4.4% | 75.37 | 75.14 | 75.29 | 0.6% | 1.21 | 0.8% |
| 50% Part to part | LM–ICP | 29.82 | 34.13 | 55.10 | 78.1% | 71.86 | 76.53 | 83.61 | 5.5% | 1.01 | 15.8% |
| | EM–ICP | 15.34 | 42.13 | 24.04 | 47.3% | 64.27 | 79.12 | 73.79 | 5.9% | 1.02 | 15.0% |
| | 4PCS | 32.23 | 31.01 | 28.43 | 10.4% | 75.13 | 75.21 | 74.31 | 1.1% | 1.21 | 0.8% |
| | 3PCHM | 30.85 | 30.43 | 31.17 | 4.8% | 75.07 | 74.35 | 74.89 | 0.8% | 1.20 | 0.0% |

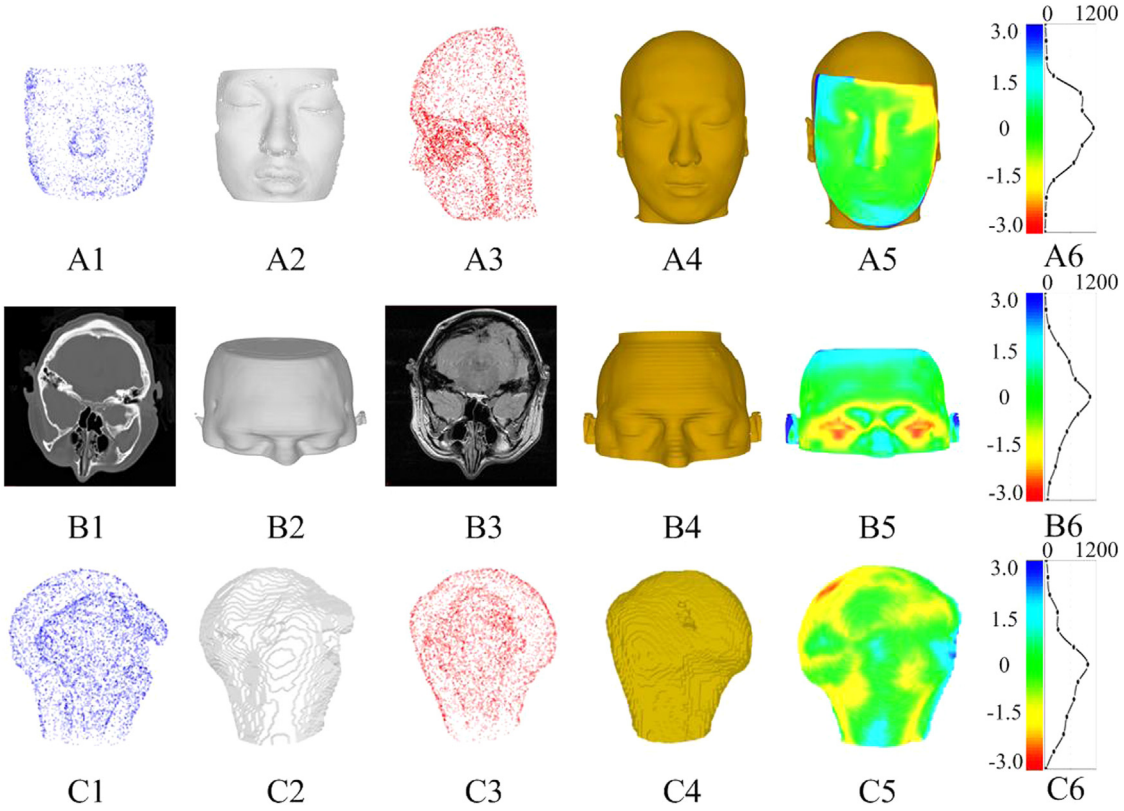


**Fig. 14.** Registration results of data sets with varying modalities. First row: A1 is the point set obtained from the 3D scanner, whereas A3 is the point set obtained from the CT image. Second row: B1 and B3 represent the CT and MRI images, respectively. Third row: C1 and C3 represent the point sets obtained from the CT image of the left and right shoulders, respectively. The first and second columns show the source data sets and their corresponding surface renderings. The third and fourth columns show the target data sets and their corresponding surface renderings. The fifth column shows the distance color map of the registered results, and the sixth column shows the color bar and the corresponding histogram of the distance errors. (For interpretation of the references to color in this figure legend, the reader is referred to the web version of this article.)

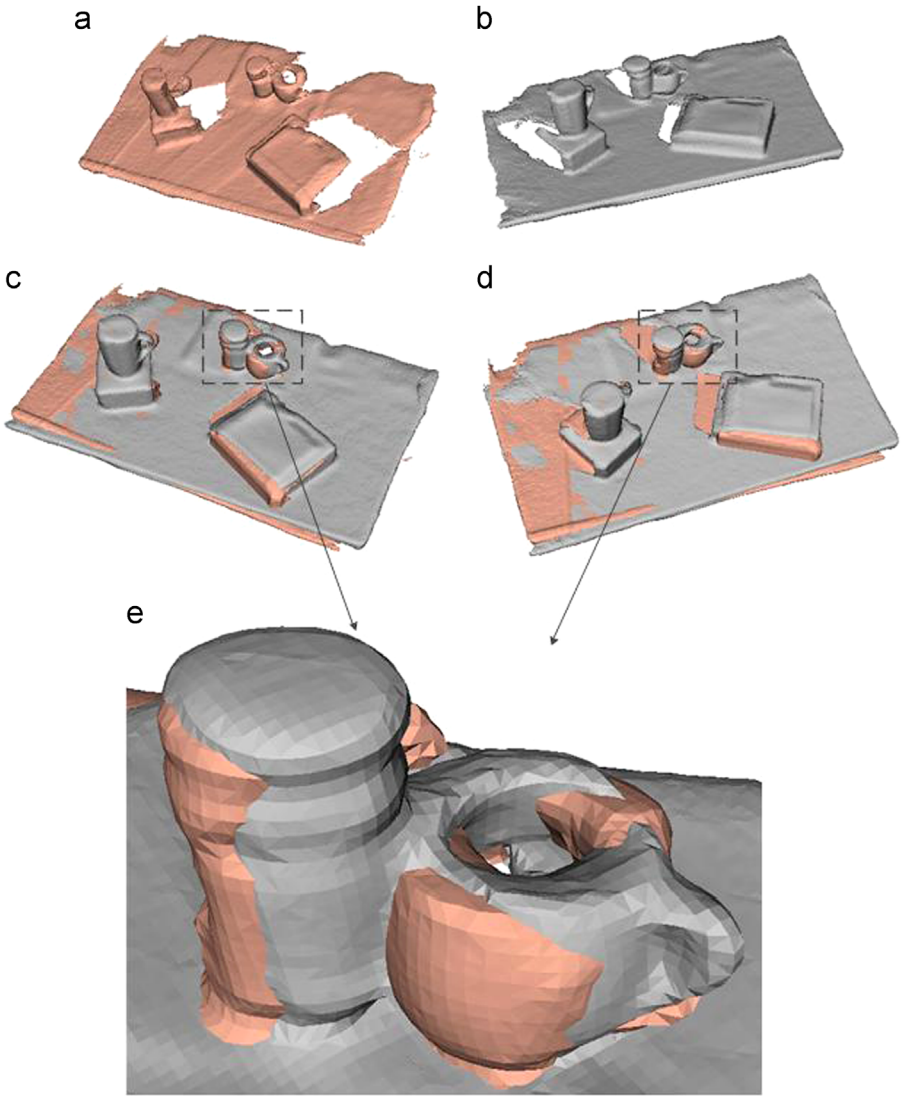


**Fig. 15.** Registration results of the table obtained via Kinect. (a) is the scene taken from the front-left view in brown. (b) is the scene taken from the front-right view in gray. (c) and (d) are the registration results. (e) is the zoomed image of the square areas in (c) and (d). (For interpretation of the references to color in this figure legend, the reader is referred to the web version of this article.)

estimation errors of the rotation and translation parameters over the $x$, $y$, and $z$ axes, whereas $\frac{|s-\hat{s}|}{\hat{s}} \cdot 100\%$ is the relative estimation error of the scaling factor. For part-to-whole registration, the result shows that the relative registration errors of rotation for LM–ICP, EM–ICP, 4PCS, and 3PCHM are 61.7%, 40.4%, 10.9%, and 4.4%, respectively. The relative errors of translation for LM-ICP, EM-ICP, 4PCS, and 3PCHM are 3.8%, 4.4%, 1.7%, and 0.6%, respectively. For part-to-part registration, the relative registration errors of rotation parameters for LM–ICP, EM–ICP, 4PCS, and 3PCHM are 78.1%, 47.3%, 10.4%, and 4.8% with corresponding relative translation errors of 3.8%, 4.4%, 1.7%, and 0.6%, respectively. For the scaling factor estimation by LM–ICP, EM–ICP, 4PCS, and 3PCHM, the relative errors are 16.7%, 19.2%, 1.7%, and 0.8% for part-to-whole registration, respectively, and 15.8, 15.0%, 0.8%, and 0.0% for part-to-part registration, respectively. Therefore, 3PCHM obtains the best estimation results of all the transformation parameters for part-to-whole and part-to-part registrations.

The proposed 3PCHM algorithm in this study is effective for the simulated point set data and can be applied flexibly to real point sets with different acquisition modalities such as MR and CT. We test the registration performance of real point sets by using the proposed algorithm (Fig. 14). We choose three different representative real data point sets for experimentation. Fig. 14(A1) and (A2) shows the point set and surface data of a human face obtained by a commonly available 3D scanner, whereas Fig. 14(A3) and (A4) shows the point set and surface data extracted from the CT data scanned by the clinical CT devices of the same person in (A1) and (A2). Fig. 14(B1) and (B3) shows two image slices of CT and MRI volume data of the same person, and these data sets have rigid transformations and are obtained from a publicly available data repository [37]. Fig. 14(C1) and (C2) shows the point set and surface data of the left shoulder bone, whereas Fig. 14(C1) and (C2) shows the point set and surface data of the right shoulder bone of the same person. The fifth column shows the corresponding registered results in the form of a distance color map, whereas the sixth column shows the color bar diagrams corresponding to the fifth column. These results are meaningful registration problems because they can be applied in real clinical scenarios for diagnostic purposes.

For the first data sets, a total of 25367 and 326548 points were extracted from the scanner data and the CT data. This result shows that for the scanner data, almost all points are distributed on the

surface of the face. For the CT data, many points are distributed inside the head (in addition to the surface of the head) because we use a simple threshold to extract the surface and the anatomic structures of the brain with the same intensity ranges. The proposed algorithm can register these two data sets together even under high noise levels, and about 92% of the total points have errors of less than 1.5 units. The second row highlights the registration of data acquired from different imaging modalities. Registering these data together is difficult because their intensity distributions are different. These two data sets are acquired at different times and contain motion artifacts. However, the proposed 3PCHM can achieve accurate initial similarity transformation estimation, which can be used to refine voxel-to-voxel non-rigid warping. For this experiment, about 94% of the total points have errors of less than 1.5 units. The third data sets are designed to register the left shoulder joint with that of the right shoulder joint. This type of registration is useful in orthopedics for the diagnosis and treatment of joint problems. Our experiment shows that about 96% of the total points have errors of less than 1.5 units. All these real data sets are registered with high accuracy. Therefore, the 3PCHM algorithm can be used for the initial pose estimation for multiple modality image registration.

Apart from the stereoscopic acquisition technology used in medical imaging, 3D real-world data is often collected by depth camera such as Kinect. The imaging principle of the depth camera decided that the image rendering is in one visual angle only; thus, registration is necessary for the joint fusion of the collected data from different imaging views. The 3PCHM approach is capable of registering real-world data collected by depth cameras even if the data is incomplete or contain large amounts of holes. Fig. 15 shows the registration result for a table data collected by Kinect. In Fig. 15 (a) and (b), we find that the original scene presents only one-sided information for the objects, that is, the reverse side of the cup and book is missing. After registration by 3PCHM, Fig. 15(c) and (d) shows the registered result rendering from two different angles. The uniform overlapping of brown and gray indicates that two models are combined properly. In the zoom inset, we show the precise fit in alignment of the 3PCHM algorithm. Fig. 16 provides another experiment on desk data experiment and shows that our algorithm aligns the scans reliably.

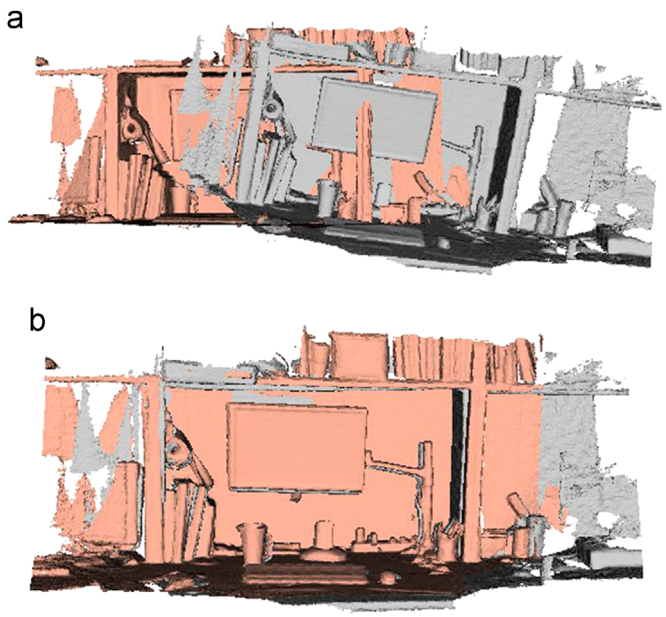


**Fig. 16.** Registration results of the desk obtained via Kinect. (a) Shows the two raw models obtained from a different views. (b) Shows the registration result.

Table 5 compares the computational times of the LM–ICP, EM–ICP, 4PCS, and 3PCHM algorithms over a different number of points. When the points in the point cloud increases from 1000 to 5000, the computational time of LM–ICP extends from 38.15 s to 293.14 s with a standard deviation of 10.19 s and a variation of 46.21s, the computational time of EM–ICP extends from 3.82 s to 31.28 s, and the computational time of 4PCS extends from 1.27s to 9.31 s. The 3PCHM algorithm achieves the best performance because its computational time ranges from 0.15 s to 2.21 s with a standard deviation of 0.03.

## 4. Conclusions

In this paper, a novel 3PCHM algorithm has been proposed for the registration of 3D point sets. The registration is conducted by using the invariant property of the 3D convex hull. The convex hull is extracted from both point sets, and potential similar triangles on the surface of the convex hull are obtained by comparing the ratios of the edges of all triangles. The initial transformation parameters are optimized by minimizing the Euclidean distance between the corresponding vertex pairs. The k-d tree algorithm is used during the calculation to classify the distance errors and to find the closest point pairs between the source and target point sets. Outliers that may cause significant errors are discarded by the RANSAC algorithm to guarantee the global optimization of the transformation parameters.

The experimental results demonstrate the effectiveness and robustness of the proposed 3PCHM algorithm for the registration of 3D point sets with similarity transformation. Compared with the widely used LM–ICP, EM–ICP, and 4PCS algorithms, 3PCHM enhances the efficiency of the registration several times even under the presence of noise and outliers. The 3PCHM algorithm also outperforms the other algorithms in special cases such as when the point set is rotated to a certain angle or when partial registration and certain levels of overlap exist. This algorithm has also demonstrated its effectiveness on both multimodality medical image data and real point sets captured by the Kinect Camera.

The proposed algorithm has the following major contributions. Considering the invariant property of 3D convex hull, the registration method is not limited to the initial pose. Moreover, alignment is quickly achieved by using the convex hull because the number of vertexes on the convex hull is smaller than the size of the point set. The proposed registration algorithm is very effective and robust for point set or model registration, as it is fully automatic, it can be utilized for various applications such as model fusion, difference quantification, object tracking and model

**Table 5**
Comparison of the time efficiency with varying registration algorithms.

| Size/Time(s)/Methods | 1000 | 2000 | 3000 | 4000 | 5000 |
|---|---|---|---|---|---|
| LM–ICP | $38.15 \pm 10.19$ | $91.34 \pm 15.44$ | $131.26 \pm 20.87$ | $194.57 \pm 37.19$ | $293.14 \pm 46.21$ |
| EM–ICP | $3.82 \pm 1.13$ | $9.72 \pm 2.02$ | $14.26 \pm 3.10$ | $21.74 \pm 3.85$ | $31.28 \pm 5.26$ |
| 4PCS | $1.27 \pm 0.37$ | $2.67 \pm 0.51$ | $4.19 \pm 1.38$ | $7.89 \pm 1.67$ | $9.31 \pm 2.19$ |
| 3PCHM | $0.15 \pm 0.03$ | $0.41 \pm 0.12$ | $0.87 \pm 0.24$ | $1.50 \pm 0.31$ | $2.21 \pm 0.43$ |

retrieval. The limitation of the proposed algorithm is that if a large number of outliers or noise or concave structure located outside of the point sets, the shapes of the convex hull of source and target points will variate significantly, and it will lead to failure registration of the point set. On the other hand, if the point set is sphere-like structure, every point in the point set could be determined as the vertex on the convex hull. In such case, the time consuming of the registration procedure will be considerably raised for the triangle facet matching. Therefore, future studies will be focused on improving the performance of the 3PCHM algorithm by using GPU-accelerated implementation or improving the degenerating conditions of the sphere-like structure.

## Acknowledgment

This work was supported by the National Basic Research Program of China (2013CB328806), the Key Projects in the National Science & Technology Pillar Program (2013BAI01B01), the National Hi-Tech Research and Development Program (2015AA043203), and the National Science Foundation Program of China (81430039, 61501030, 31200708).

## References

[1] P.J. Besl, N.D. McKay, A method for registration of 3-D shapes, IEEE Trans. Pattern Anal. Mach. Intell. 14 (1992) 239–256.
[2] S. Granger, X. Pennec, Multi-scale EM-ICP: a fast and robust approach for surface registration, in: Proceedings of the 7th European Conference on Computer Vision – ECCV, Part IV, Berlin, Germany, 28–31 May, 2002, pp. 418–32.
[3] S. Granger, X. Pennec, A. Roche, Rigid point-surface registration using an em variant of ICP for computer guided oral implantology, in: Proceedings of the Medical Image Computing and Computer-Assisted Intervention – MICCAI, vol. 2208, 2001, pp. 752–761.
[4] A. Myronenko, S. Xubo, Point set registration: coherent point drift, IEEE Trans. Pattern Anal. Mach. Intell. 32 (2010) 2262–2275.
[5] A. Myronenko, X. Song, M.A. Carreira-Perpinán, Non-rigid point set registration: Coherent point drift, Advances in Neural Information Processing Systems, (2007) 1009.
[6] B. Jian, B.C. Vemuri, Robust point set registration using gaussian mixture models, IEEE Trans. Pattern Anal. Mach. Intell. 33 (2011) 1633–1645.
[7] B. Combes, S. Prima, Prior affinity measures on matches for ICP-like nonlinear registration of free-form surfaces, IEEE International Symposium on Biomedical Imaging: From Nano to Macro, ISBI '09, 2009, pp. 370–373.
[8] J. Goldberger, S. Gordon, H. Greenspan, An efficient image similarity measure based on approximations of KL-divergence between two gaussian mixtures, in: Proceedings of the IEEE International Conference on Computer Vision, vol. 1, 2003, pp. 487–493.
[9] G.C. Sharp, S.W. Lee, D.K. Wehe, ICP registration using invariant features, IEEE Trans. Pattern Anal. Mach. Intell. 24 (2002) 90–102.
[10] C. Schutz, T. Jost, H. Hugli, Multi-feature matching algorithm for free-form 3D surface registration, in: Proceedings of the Fourteenth International Conference on Pattern Recognition, 1998, pp. 982–984.
[11] J. Feldmar, N. Ayache, Rigid, affine and locally affine registration of free-form surfaces, Int. J. Comput. Vis. 18 (1996) 99–119.
[12] S. Rusinkiewicz, M. Levoy, Efficient variants of the ICP algorithm, in: Proceedings of the Third International Conference on 3-D Digital Imaging and Modeling, 2001, pp. 145–152.
[13] D. Aiger, N.J. Mitra, D. Cohen-Or, 4-Points congruent sets for robust pairwise surface registration, ACM Trans. Graph. (TOG) (2008) 85.
[14] G. Mori, S. Belongie, J. Malik, Efficient shape matching using shape contexts, IEEE Trans. Pattern Anal. Mach. Intell. 27 (2005) 1832–1837.
[15] S. Belongie, J. Malik, J. Puzicha, Shape matching and object recognition using shape contexts, IEEE Trans. Pattern Anal. Mach. Intell. 24 (2002) 509–522.
[16] A.E. Johnson, M. Hebert, Using spin images for efficient object recognition in cluttered 3D scenes, IEEE Trans. Pattern Anal. Mach. Intell. 21 (1999) 433–449.
[17] R. Sara, I.S. Okatani, A. Sugimoto, Globally convergent range image registration by graph kernel algorithm, in: Proceedings of the Fifth International Conference on 3-D Digital Imaging and Modeling, 3DIM, 2005, pp. 377–384.
[18] T. Masuda, Log-polar height maps for multiple range image registration, Comput. Vis. Image Underst. 113 (2009) 1158–1169.
[19] Y. Liu, Automatic registration of overlapping 3D point clouds using closest points, Image Vis. Comput. 24 (2006) 762–781.
[20] S. Gold, A. Rangarajan, C.-P. Lu, S. Pappu, E. Mjolsness, New algorithms for 2d and 3d point matching: pose estimation and correspondence, Pattern Recognit. 31 (1998) 1019–1031.
[21] L. Maier-Hein, Convergent iterative closest-point algorithm to accomodate anisotropic and inhomogenous localization error, IEEE Trans. Pattern Anal. Mach. Intell. (2012).
[22] A.W. Fitzgibbon, Robust registration of 2D and 3D point sets, Image Vis. Comput. (2003) 1145–1153.
[23] R. Sandhu, S. Dambreville, A. Tannenbaum, Point set registration via particle filtering and stochastic dynamics, IEEE Trans. Pattern Anal. Mach. Intell. vol. 32 (2010) 1459–1473.
[24] R. Sandhu, S. Dambreville, A. Tannenbaum, Particle filtering for registration of 2D and 3D point sets with stochastic dynamics, in: Proceedings of the IEEE Conference on Computer Vision and Pattern Recognition, CVPR, 2008, pp. 1–8.
[25] G. Blais, M.D. Levine, Registering multiview range data to create 3D computer objects, IEEE Trans. Pattern Anal. Mach. Intell. 17 (1995) 820–824.
[26] T. Jost, H. Hugli, A multi-resolution ICP with heuristic closest point search for fast and robust 3D registration of range images, in: Proceedings of the Fourth International Conference on 3-D Digital Imaging and Modeling, 3DIM, 2003, pp. 427–433.
[27] M.A. Fischler, R.C. Bolles, Random sample consensus: a paradigm for model fitting with applications to image analysis and automated cartography, Commun. ACM 24 (1981) 381–395.
[28] S. Irani, P. Raghavan, Combinatorial and experimental results for randomized point matching algorithms, Comput. Geom. 12 (1999) 17–31.
[29] C. Papazov, D. Burschka, An efficient RANSAC for 3D object recognition in noisy and occluded scenes, in: R. Kimmel, et al., (Eds.) Proceedings of the Computer Vision-Accv 2010, Pt. I, vol. 6492, 2011, pp. 135–148.
[30] J. Jiang, J. Cheng, X. Chen, Registration for 3-D point cloud using angular-invariant feature, Neurocomputing 72 (2009) 3839–3844.
[31] T. Tamaki, M. Abe, B. Raytchev, K. Kaneda, Softassign and EM-ICP on GPU, in: Proceedings of the 3rd Workshop on Ultra Performance and Dependable Acceleration Systems, 2010, pp. 179–183.
[32] K.A. Mohamed, C. Kupich, An O ($n$ log $n$) output-sensitive algorithm to detect and resolve conflicts for 1D range filters in router tables, Albert-Ludwigs-Universität Freiburg, Technical Report , 226, 2006.
[33] The Stanford 3D Scanning Repository, Stanford. Available: ⟨http://graphics.stanford.edu⟩.
[34] S. Umeyama, Least-squares estimation of transformation parameters between two point patterns, IEEE Trans. Pattern Anal. Mach. Intell. 13 (1991) 376–380.
[35] S. Arya, D.M. Mount, N.S. Netanyahu, R. Silverman, A.Y. Wu, An optimal algorithm for approximate nearest neighbor searching fixed dimensions, J. ACM 45 (1998) 891–923.
[36] Aim@Shape, AIM@SHAPE Shape Repository v4.0, October 2015, Available: ⟨http://shapes.aimatshape.net⟩.
[37] MIDAS, Retrospective Image Registration Evaluation Database [Online]. Available: ⟨http://www.insight-journal.org/midas/⟩.

**Jingfan Fan** received his B.Sc. degree in optical engineering from the Beijing Institute of Technology in 2010. He is currently a Ph.D. student in the School of Optoelectronics, Beijing Institute of Technology, China. His research interests include medical image processing, computer vision and augmented reality.

**Jian Yang** received his Ph.D. degree in optical engineering from the Beijing Institute of Technology in 2007. He was a postdoctoral research fellow with the Mouse Imaging Centre, Hospital for Sick Children, Toronto, Canada, from 2007 to 2009. He is currently an associate professor with the School of Optoelectronics, Beijing Institute of Technology, China. He focuses his research interests on medical image processing, augmented reality, and computer vision.

**Feng Lu** received the B.S. and M.S. degrees in automation from Tsinghua University, in 2007 and 2010, respectively, and the Ph.D. degree in information science and technology from The University of Tokyo, in 2013. After working with the Institute of Industrial Science, the University of Tokyo, he joined the Beihang University in 2015. His research interests include shape recovery, reflectance analysis and human gaze estimation.

**Danni Ai** received the M.E. and B.E. degrees from Xi'an Jiaotong University in 2008 and 2005, and the D.E. degree from Ritsumeikan University, Japan, in 2011. Before joining Beijing Institute of Technology as a postdoctoral research fellow in December 2013, she was a researcher in Hitachi (China) Research & Development Corporation, Shanghai since July 2012, and a postdoctoral research fellow in Ritsumeikan University and OMRON Social Solutions Co. Ltd., Kyoto, Japan from December 2011 to June 2012. Her research interests include medical image analysis, visual feature extraction, image annotation, virtual reality and augmented reality.

**Yitian Zhao** is a lecturer at the Beijing Institute of Technology, China. He obtained his Ph.D. degree in computer science from Aberystwyth University, United Kingdom, in 2013. From November of 2013 to October 2014, he worked as a research assistant at The University of Liverpool. His primary research interests lie in 2D/3D image processing, medical image analysis, pattern recognition, computer graphics, and data-base and knowledge base systems.

**Yongtian Wang** received his B.Sc. degree in precision instrumentation from Tianjin University, China, in 1982, and his Ph.D. degree in optics from the University of Reading, England, in 1986. He is currently a Yangtze River Scholar of the Chinese Ministry of Education, a professor and the director of the Center for Research on Optoelectronics and Information Technology in Beijing Institute of Technology. His research interests include optical design and CAD, optical instrumentation, image processing, virtual reality (VR) and augmented reality (AR) technologies and applications.